Electrostatic self-assembly bmSi@C/rGO composite as anode material for lithium ion battery

CrossMark

Qiuli Li, Dingqiong Chen, Kun Li, Jing Wang, Jinbao Zhao*

State Key Laboratory of Physical Chemistry of Solid Surfaces, Collaborative Innovation Center of Chemistry for Energy Materials, College of Chemistry and Chemical Engineering, Xiamen University, Xiamen, 361005, China

A B S T R A C T

A facile and efficient electrostatic-assembly method to fabricate ball-milling-silicon@carbon/reduced-graphene-oxide composite (bmSi@C/rGO) has been developed. In the fabrication process, chitosan (CTS), as a charged bridge, connected ball milling silicon (bmSi) and graphene oxide (GO), and then was transformed into carbon coating by heat treatment. The carbon coated ball milling silicon (bmSi@C) particles were distributed evenly between the sheets of reduced graphene oxide (rGO). Therefore, the carbon coating and the wrinkled graphene sheets formed a superior conductive matrix and a buffer zone. The composite used as anode material exhibited high reversible capacity of 935.77 mAh g^{-1} and 71.9% capacity retention after 100 cycles. The excellent electrochemical properties are attributed to the well-designed structure, in which both the carbon layer and the rGO play an important role for improving the whole electrical conductivity and preventing the silicon from pulverization.

© 2016 Elsevier Ltd. All rights reserved.

1. Introduction

The development of lithium ion batteries with superior electrochemical performance, such as high energy density and long cycle life, as we know, is of vital importance for various portable electronic products, especially for the hybrid electronic vehicles (HEV) and electronic vehicles (EV) [1]. Lots of efforts have been devoted to seeking promising electrode materials, in which silicon is one of favorable materials. It is greatly identified that silicon has the most lithium ion storage capacity (4200 mAh g^{-1}) when lithiated to Li$_{4.4}$Si, which is more than ten times of the current graphite (372 mAh g^{-1}) [2]. Furthermore, it has a low discharge voltage and is of great storage in the earth as well as environmental friendly. However, there still exist some self-restrictive problems to be solved for commercial application. For example, silicon particles expand and impinge on each other sharply in lithiation, but contract instead in delithiation, resulting in the pulverization and detachment of the active materials from the current collector and rapid decrease of the capacity [3]. Also, the rate performance will be poor since silicon is a semi-conductor with poor intrinsic electrical conductivity [4].

There are various methods proposed for improving the defects of silicon, in which the carbon coating seems an effective way [5].

The carbon coating will improve not only the conductivity but also the giant volume change and the intimacy of the particles for the silicon/carbon composite [6]. Recently, as a particular carbon material, graphene has attracted extensive attention. Graphene possesses large specific surface, superior electron conductivity and mechanical flexibility [7]. Therefore, the silicon/graphene composite could take a strong effect in buffering the volume change in the lithiation-delithiation processes. The inherent flexibility and large sheet surfaces, on the other hand, could make it to form a 3D conductive network in the composite [8].

It is of particular value to fabricate silicon/carbon or graphene composite. The electrostatic assembly is a better one of the composite structure assembly methods because of easy-operating and immediate reacting [9,10]. Zhou et al. [11] synthesized Si/rGO composite by electrostatic assembly between positively charged aminopropyltriethoxysilane (APS) modified Si nanoparticals and negatively charged graphene oxide, followed by thermal reduction. The APS modification was also applied to other cases [12,13] and materials, such as metal oxides [14,15] and SiO2 [16] to get the positively charged particle surfaces. Some cationic polymers were also employed in the assembly processes, for example, Zhou et al. [17] synthesized Si/rGO by converting the negatively charged surfaces of silicon particles to positively charged surfaces via adsorption of polydiallyldimethylammoniumchloride (PDDA), as a result, the electrostatic assembly was performed between the PDDA-Si and the negatively charged rGO. Conversely, Lim et al. [18]

used PDDA to modify the reduced graphene oxide for being positively charged and then the electrostatic assembly was achieved between PDDA-rGO and Li-rich cathode. Little carbon residue can be found in the all above cases. Lin et al. [19] fabricated Si@C/rGO composite assisted by polymerization of aniline on the surfaces of silicon particles, in which the polyaniline (PANI) coating would guarantee the assembly of GO and Si-PANI, and PANI could be transformed into carbon layer by heat treatment. However, the polymerization process is under strict conditions and time-consuming. Therefore, it is necessary to develop an easy-operating, time-saving and successive method to fabricate a Si@C/rGO composite.

In this work, bmSi was used as the raw material for low cost, high yield and simple process. Both the carbon and graphene were combined as dual protective network in the bmSi@C/rGO composite through two-step successive deposition processes driven by electrostatic interactions at ambient temperature as Fig. 1 shown. Firstly, the chitosan is chosen as carbon source because, when it dissolves in an acidic liquid, it will possess positive charge as a result of protonation of amino groups [20,21]. Once the chitosan is attached on the surfaces of silicon particles through electrostatic interaction, by adjusting the pH value of the silicon@chitosan (bmSi@CTS) dispersion, a positively charged surface will be achieved again since the protonation of the rest amino groups [20]. At the same time, the agglomeration between the silicon particles can be avoided. Graphene oxide possess a negative charge over a broad pH range due to the ionization of the dangling carboxylic acid and phenolic hydroxyl groups [14]. Thus, another electrostatic interaction procedure will proceed between the bmSi@CTS composite and graphene oxide. In the process the GO composite will encompass and interconnect the bmSi@CTS particles as a resule of the the superior flexibility and large surface area of GO. Finally, the bmSi@C/rGO was produced through a process of in-situ carbon thermal reduction. In the assembly structure, both the carbon and reduced graphene oxide play important roles in enhancing the whole electrical conductivity and buffering the volume expansion of silicon during the lithiation-delithiation process. When used as anode material, superior electrochemical performance is displayed. Definitely, as-prepared bmSi@C/rGO delivers a high reversible capacity of 935.77 mAh g^{-1} and 71.9% capacity retention after 100 cycles while the capacity of bmSi particles drops sharply down to 75.23 mAh g^{-1} under the same test conditions.

2. Experimental

All commercial chemicals used in this work are analytical grade (AR) and not further purified before using. The graphene oxide was prepared by a modified Hummer's method [22]. The chitosan solution was prepared by dissolving 1.0 g chitosan powders into 100 mL of 5% (v/v) acetic acid aqueous solution.

2.1. Preparation of bmSi particles

The commercial available silicon (Huierna, 200 mesh) was ball-milled with deionized water as solvent. The ball-milling process was conducted with a rotating speed of 400 rpm for 24 h. And then the obtained products were washed with 10 wt% HF for several minutes and dried at 80 °C under vacuum condition.

2.2. Preparation of bmSi@C/rGO composite

Firstly, 0.1 g of the prepared bmSi was evenly dispersed into 50 mL absolute ethyl alcohol by ultrasonication for 30 min. Then 6 mL of CTS solution was injected into the above system and the pH value of the system was kept to be around 3.0 by addition of 1 M HCl. When the injection finished, the system was dispersed by IKA disperser for 5 min. The bmSi@CTS particles were obtained after centrifuging and washing away the untightly absorbed CTS with absolute ethyl alcohol. Then bmSi@CTS particles were dispersed into 50 mL ethyl alcohol, followed that 20 mL of 5.0 mg mL^{-1} GO aqueous solution was added into the system drop by drop under pH value of about 3.0 adjusted by 1 M HCl. Stirring the suspension for 30 min, we obtained the bmSi@CTS/GO by centrifuging and washing. The transformation of the reactive system was shown in Fig. 2b. Finally, the bmSi@C/rGO was prepared by thermal treatment of bmSi@CTS/GO at 700 °C for 3 h under argon atmosphere with 5% H$_2$. For comparison, bmSi@C was synthesized with the same method except for the second electrostatic procedure.

2.3. Characterization

The particle size distribution was measured on the Laser Particle Size Analyzer (90 Plus PALS, Brookhaven). The Fourier-transformed infrared (FT-IR) spectrum was measured on a Nicolet 330 infrared spectrometer in transmittance mode over the range of 400–4000 cm^{-1}. X-ray diffraction (XRD) patterns were obtained on a Rigaku miniflex 600 instrument using Cu Kα radiation (λ = 0.154 nm). Raman spectra were tested on JOBIN Yvon Horiba Raman Spectrometer model HR800 with 532 nm diode laser excitation. Besides, morphologies of the samples were characterized by field emission scanning electron microscopy (SEM, HITACHI S-4800) and transmission electron microscopy (TEM, JEOL-2100). In order to quantify the element content, thermal gravimetric analysis (TGA) was conducted on SDT Q600 system (TA Instrument).

2.4. Electrochemical measurements

Electrochemical performance was measured in the form of CR2016 coin-type cell in which a voltage range of 0.02–1.5 V (vs. Li/Li$^+$) was employed. The half cell, which includes the working
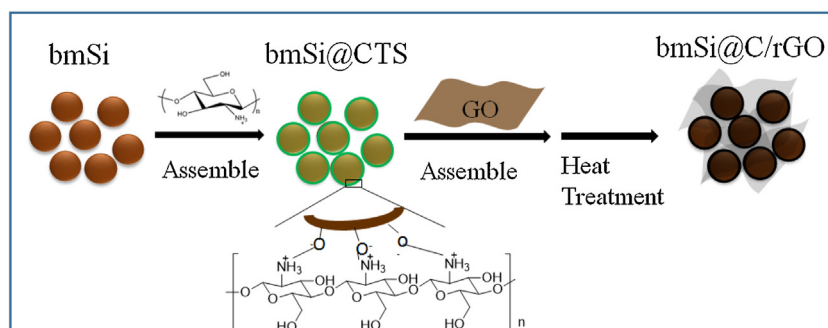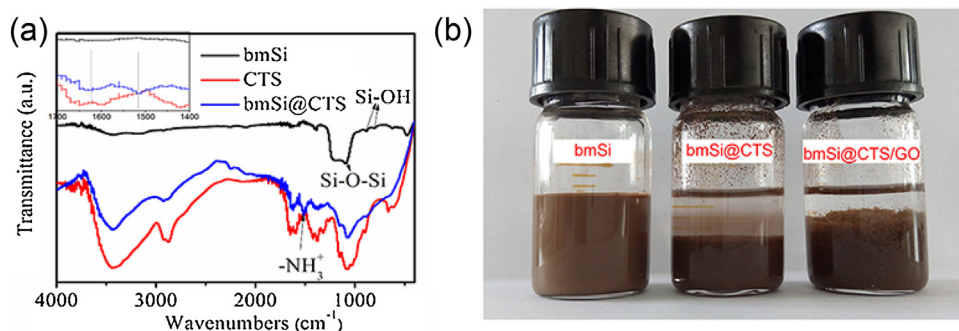

Fig. 1. The scheme for the preparation of bmSi@C/rGO composite.

Fig. 2. (a) FT-IR spectra of the bmSi, CTS and bmSi@CTS particles. (b) The photographs of bmSi suspension, bmSi@CTS precipitate and bmSi@CTS/GO precipitate.

electrode involved and high-purity lithium metal as the counter electrode, was assembled in the argon-filled glove box. 1 M $LiPF_6$ and 5 wt% fluoroethylene carbonate (FEC) additives dissolved in a mixture of ethylene carbonate (EC)/dimethyl carbonate (DMC)/ diethyl carbonate (DEC) (1:1:1 in volume ratio) were served as the electrolyte. Celgard2400 polyethylene was employed as the separator. Using deionized water as the solvent, the working electrode was obtained by spreading a uniform slurry containing 60 wt% active material, 30 wt% acetylene black (AB), 10 wt% bi-component binder of same weight ratio of carboxyl methyl cellulose (CMC) and styrene-butadiene resin (SBR) onto the copper foil current collector. The coating thickness and mass loading of the electrodes in study were in Table S1 (Supporting information).

The cells were galvanostatically charged and discharged on a battery test system (NEWARE BTS type battery charger, Shenzhen, China) between 0.02 and 1.5 V at 25 °C. The specific capacity was calculated based on the total weight of composite contained in the cathode.

Cyclic voltammogram (CV) measurement was performed on a CHI660D potentiostat at a scan rate of 0.1 mV s^{-1} with a voltage range of 0.01–1.5 V (vs Li/Li$^+$). Electrochemical impedance spectra (EIS) were measured at open-circuit voltage with the frequency ranging from 100 kHz to 0.01 Hz (Solartron SI 1287).

3. Results and discussion

The FT-IR spectra of the bmSi, CTS and bmSi@CTS particles are showed in Fig. 2a. A series of characteristic bands appear in the spectrum of bmSi particles, such as Si-O-Si (1080 cm^{-1}) and Si-OH (945 cm^{-1}) stretching vibration, which demonstrate the existence of SiO$_x$ on the surfaces of the bmSi particles and it is very important for the first assembly process. In the spectrum of the bmSi@CTS composite, the absorbance band of Si—OH disappears. Further-more, a set of new bands related to the absorbance of chitosan can be detected. Except the above bands, the absorption peaks at about

1623 cm^{-1} and 1519 cm^{-1} associated with the stretching of NH$_3^+$ [23,24] are particularly prominent. Thus, we can get the conclusion that chitosan is adsorbed onto the bmSi particles through the electrostatic interaction between —OH and —NH$_3^+$ in an acid system. As Fig. 2b shown, after chitosan solution was added into the evenly-dispersed silicon-ethanol solution under acid circum-stance, precipitates formed from the system. Accordingly, the surfaces of the particles are transferred from negatively charged bmSi to positively charged bmSi@CTS once in an acid medium. This provides necessary condition for next assembly step. Correspond-ingly, Fig. 2b conveys that new precipitates marked as bmSi@CTS/ GO come into being in the bmSi@CTS and GO suspension.

After thermal reduction of bmSi@CTS and bmSi@CTS/GO, we obtain bmSi@C and bmSi@C/rGO composites, respectively. The XRD patterns of bmSi particles, bmSi@C and bmSi@C/rGO composites are shown in Fig. 3a. It can be detected that all of the three patterns exhibit the same main diffraction peaks located at 28.5°, 47.3° and 56.1°, which can be indexed to the lattice plane of (111), (222) and (331) for cubic crystalline silicon. Beyond that, there is a broad diffraction peak at 25.0° for bmSi@C and a definite peak at 26.0° for bmSi@C/rGO particles, which indicate the existence of amorphous carbon and stacking of graphene sheets, respectively [25]. From the EDS (Fig. S1, Supporting Information) of the bmSi@C composites, the carbon element emerges with the appearance of Si and O. We can conclude that through the electrostatic interaction and in-situ carbonization, chitosan is transferred into carbon coating on the silicon particles. To further prove the feasibility of the design solution, Raman spectra of the relevant composites are collected in Fig. 3b. The strong peak at about 517 cm^{-1} appears in all of the Raman spectra and it is associated with the characteristic peak of pure silicon. Additional-ly, the broad peaks at 1355 and 1600 cm^{-1} in bmSi@C and bmSi@C/ rGO are attributed to disorder-induced D band and the graphitic G band of the carbon structure [26]. Usually, The D band is considered to be from the disordered structure of amorphous
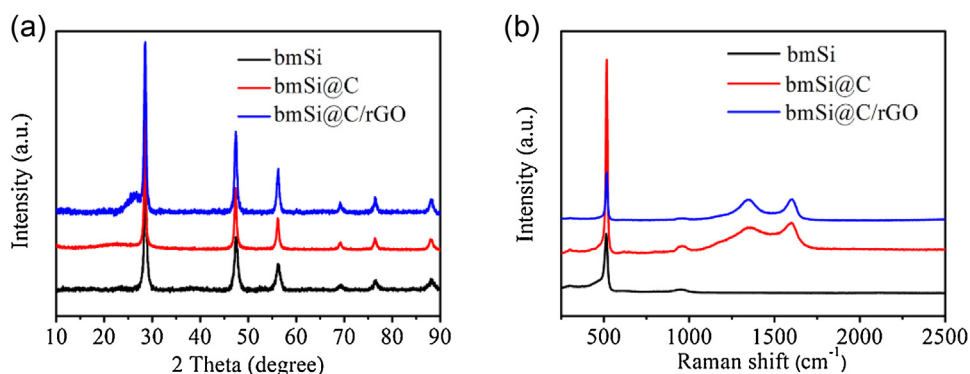
Fig. 3. (a) XRD patterns of the bmSi, bmSi@C and bmSi@C/rGO particles. (b) Raman spectra of the bmSi, bmSi@C and bmSi@C/rGO particles.

carbon or edge flaw of graphite structure, while G band is in agreement with the ordered graphitized structure [27]. The intensity ratio of D band and G band is increased from 0.91 of bmSi@C to 0.98 of bmSi@C/rGO as a result of the reduction of GO to rGO [28]. Thus, we can conclude that the design solution is successfully achieved and a conducting network composed of amorphous carbon derived from chitosan and graphitized carbon relating to the graphene sheets is brought about in the bmSi@C/rGO composite. The TGA curves of the relevant composites are collected in Fig. S2 (Supporting Information). Accordingly, the mass content of bmSi, C and rGO in the bmSi@C/rGO composite is 66.7%, 12.9% and 20.4%, respectively.

Fig. 4a displays SEM of bmSi particles, it can be detected that the silicon particles made by ball milling method possesses irregular morphology and rough surface. And for the reason that the bmSi particles go through abstersion by HF in the process of preparation, there exists an imbalance in the bulk phase (Fig. S3, Supporting Information). Moreover, no obvious agglomeration can be found. The particle size distribution (Fig. S4, Supporting Information) revealed that the diameter of bmSi particles ranges from 71.8 nm to 349.1 nm, and the average diameter of bmSi is 177.7 nm. After the bare silicon is coated by chitosan and in-situ carbonized, the composite presents the morphology as shown in Fig. 4b. Nothing distinct difference can be identified in the morphology compared with that of pure bmSi particles. During the preparation of bmSi@C/rGO, the GO envelops and interconnects the bmSi@CTS particles into large bulk as for its large specific surface area and good flexibility. It can be found in Fig. 4c that most Si@C particles are connected by the wrinkled rGO nanosheets, while few are exposed on the rGO surfaces. The bmSi@C particles are evenly dispersed between the sheets of rGO. And Fig. 4d showed that the rGO is not only coating on the outside of agglomeration of bmSi@C particles, but also connecting and shuttling between the bmSi@C particles. So, rGO made the composite integral to provide a relative steady structure. The flexibility and wrinkles of rGO associating carbon coating on the bmSi particles provide a supreme conductive martrix in the composite. We can find in the inset in Fig. 4e that the thickness of carbon coating is about 5 nm.

The first charge-discharge voltage profiles of initial cycle of the electrodes made from as-prepared composites and pristine silicon at a current density of $0.2 \, A \, g^{-1}$ in the potential range of 0.02–1.5 V (vs. Li/Li$^+$) are shown in Fig. 5a. The discharge voltage plateaus at about 0.1 V for the three electrodes can be attributed to the lithiation of silicon. The bmSi, bmSi@C and bmSi@C/rGO deliver

discharge capacity of $3795.0 \, mAh \, g^{-1}$, $2325.5 \, mAh \, g^{-1}$ and $2126.8 \, mAh \, g^{-1}$, respectively. Accordingly, the initial coulombic efficiency is 68.06%, 75.08% and 66.60% in sequence. Fig. 5b illustrates the charge-discharge curves of bmSi@C/rGO electrode in specific cycles at the current density of $0.2 \, A \, g^{-1}$. The short plateau at about 0.8 V in the first discharge process is absent in the following cycles, which is associated with the electrochemical deposition of electrolyte on the surfaces of active particles [29]. Additionally, a slightly charge capacity increase appears in the fifth cycle compared with that of the first cycle. This is caused by gradual activation process as other cases explained [5]. In the following cycles, the curves shift slowly to lower capacity, which means good cycling behavior.

Fig. 5c displays the cycling behavior of the electrodes involved at a current density of $0.2 \, A \, g^{-1}$ in the potential range of 0.02–1.5 V. The bmSi delivers the highest initial capacity, $2558.5 \, mAh \, g^{-1}$, but it drops rapidly to $73.6 \, mAh \, g^{-1}$ after 100 cycles. Such phenomenon can be also found in other case [30]. This is attributed to the poor electronic conductivity and the drastic volume expansion during the lithiation/delithiation process. When the bmSi particles are coated with carbon layer, the resulted bmSi@C shows a slight improvement in the cycle performance. As expected, it is the bmSi@C/rGO that exhibits the most outstanding cycling stability. A capacity of $935.77 \, mAh \, g^{-1}$ is retained after 100 cycles. Furthermore, the coulombic efficiency increases rapidly to >95% and keeps steady in the rest cycles.

All the above imply that the existence of C and rGO decreases the capacity of the electrode for the non-active property, but C coating improves the coulombic efficiency while rGO pushes it down as the inherent initial irreversible capacity loss of rGO [11,31]. There are other data (Fig. S5, Supporting Information) provided convincing evidences for this opinion. When the ratio of GO to bmSi increases from 1:2, 1:1 to 2:1 (marked as 1:2, 1:1, 2:1, respectively), the specific capacity and the initial coulombic efficiency decreases correspondingly while the cycle performance improves gradually. As regards of the 1:2 composite, we etched part of the active silicon by 10 wt% HF for 5 min, noted as 1:2-HF. The relative content of rGO in the 1:2-HF is lowered down as a consequence. Comparing the electrochemical performance of the 1:2 to the 1:2-HF (Fig. S6, Supporting Information), it can be found that the capacity and initial coulombic efficiency of the 1:2-HF are at a relatively low level, however, the cycling performance is greatly strengthened. Hence, we can draw a conclusion that the rGO may bring down the capacity and initial coulombic efficiency,
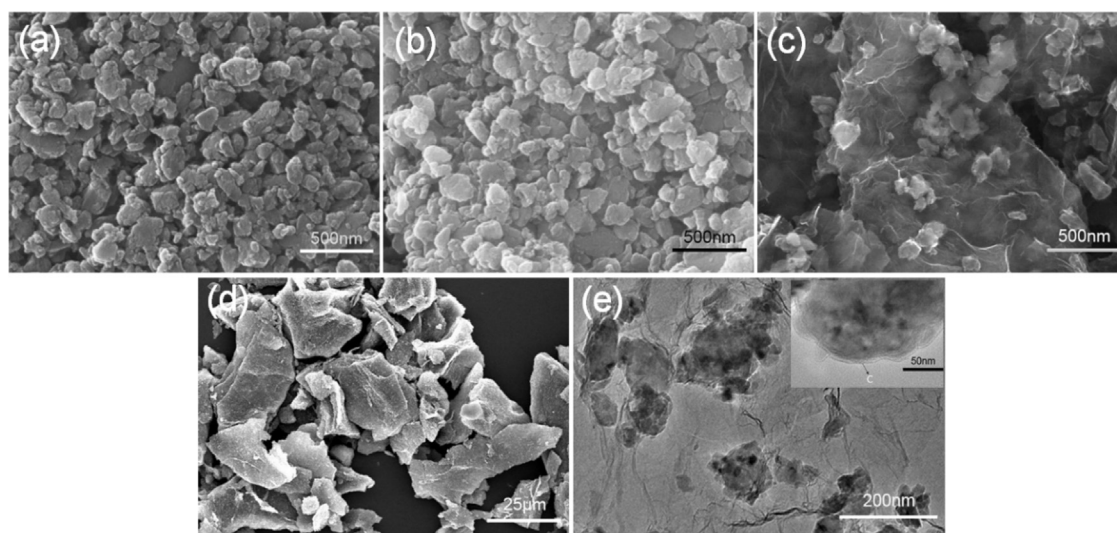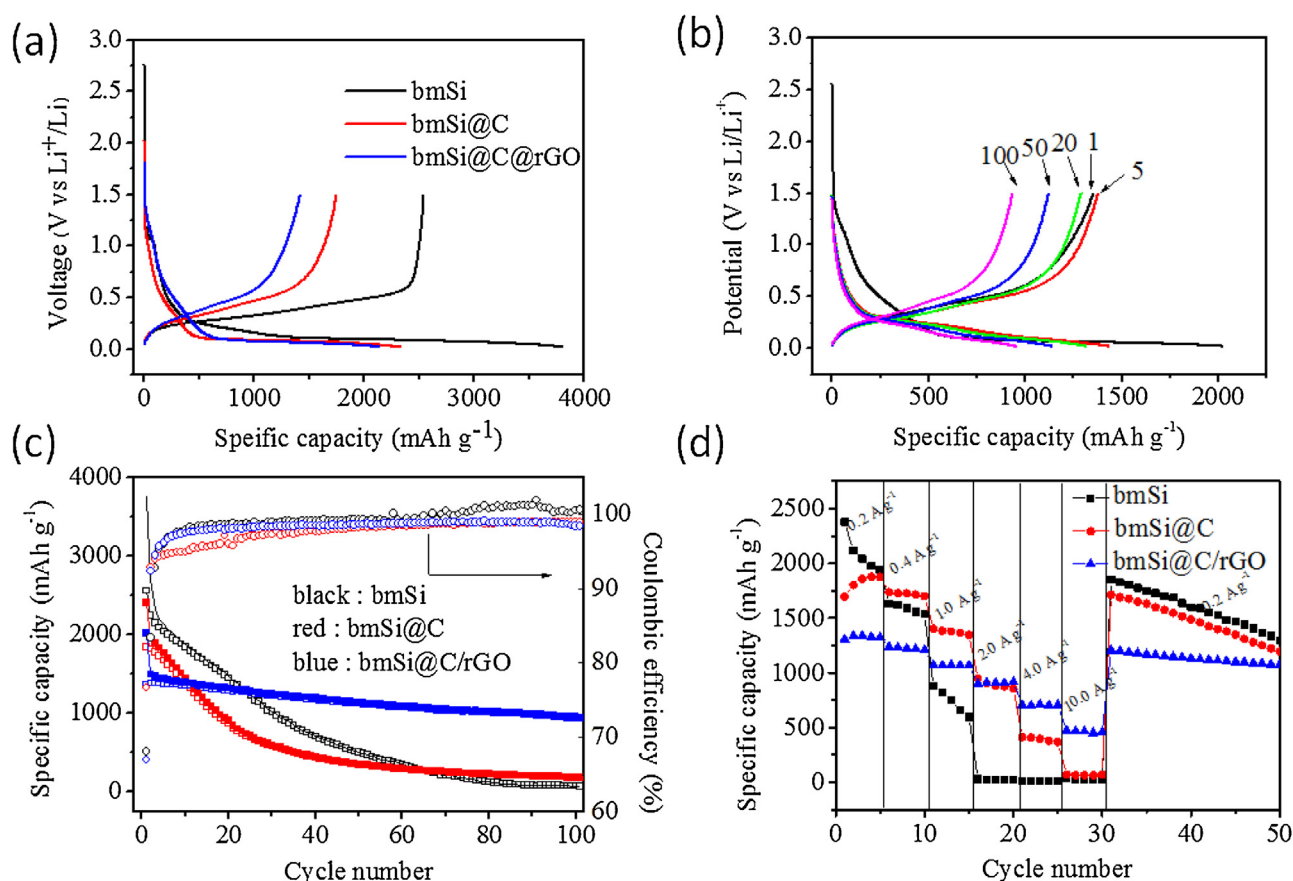

Fig. 4. SEM images of enlarged (a) bmSi, (b) bmSi@C, (c) bmSi@C/rGO, (d) general view of bmSi@C/rGO. (e) TEM images of bmSi@C/rGO.

Fig. 5. (a) Initial discharge-charge voltage profiles of bmSi, bmSi@C, and bmSi@C/rGO. (b) Discharge-charge voltage profiles of bmSi@C/rGO at a current density of 0.2 A g^{-1} of 1st, 5th, 20th, 50th, and 100th. (c) Cycling performance of the bmSi, bmSi@C, and bmSi@C/rGO electrodes at a current density of 0.2 A g^{-1}. (d) Rate performance of bmSi, bmSi@C, and bmSi@C/rGO composite.

but it is very important for improving the cycling performance of the composite[32]. And it should be clear that moderate AB is necessary for its strengthening the electron conduction by providing more point-to-point sites in the composite electrode, thus the polarization would be reduced and the coulombic efficiency during the cycling would be at a higher level [33] (Fig. S7, Supporting Information).

Fig. 5d exhibits the rate performance of the three electrodes at the current densities ranging from 0.2 A g^{-1} to 10.0 A g^{-1} and returning to 0.2 A g^{-1} at last. The specific capacity of the electrode made from bmSi decreases sharply to 500.0 mAh g^{-1} or lower when the current densities increase to larger than 1.0 A g^{-1}. The

bmSi@C/rGO electrode has an average capacity of 1326.5, 1224.7, 1069.4, 908.2, 706.6 and 464.3 mAh g^{-1} at the current densities of 0.2, 0.5, 1.0, 2.0, 5.0, 10.0 A g^{-1}, respectively. When the current density returns to 0.2 A g^{-1}, a capacity of 1205.1 mAh g^{-1} can be regained, which implies a favorable reversibility and rate performance. The lower capacity of bmSi@C/rGO at the lower current densities is due to that the active silicon content in bmSi@C/rGO is lower than that of bmSi@C.

The cyclic voltammetry (CV) curves of the bmSi@C/rGO electrode of first five cycles between the potential range of 0.01–1.5 V (vs Li$^+$/Li) are revealed in Fig. 6a. There is a noteworthy cathodic peak at about 1.1 V in the first cathodic process. Generally,
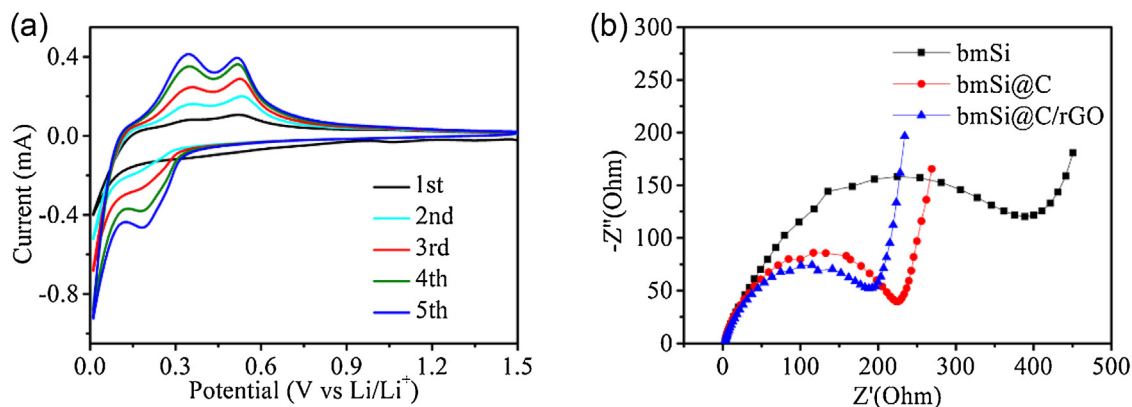
Fig. 6. (a) Cyclic voltammetry curves of the bmSi@C/rGO electrode of first five cycles. (b) Nyquist plots of the bmSi, bmSi@C, and bmSi@C/rGO electrodes.

it is triggered by the formation of solid electrolyte interphase (SEI) that will disappear in the following cycles. It is the process that gives rise to the loss of irreversible capacity and the lower initial coulombic efficiency. The cathodic peak at 0.1 V shifts gradually to 0.2 V as a result of phase transformation of crystalline silicon to amorphous silicon [34] and it is assigned to the lithiation reaction. It is noteworthy that there are two anodic peaks associating with delithiation of silicon in the anodic process. The strengthening of the peaks is in accordance with increase of charge capacity in the first few cycles as Fig. 5b exemplified, which is ascribed to the activation process [35].

The enhanced electrical conductivity can be demonstrated by electrochemical impedance spectroscopy (EIS). As Fig. 6b revealed, the Nyquist plots for bmSi, bmSi@C, bmSi@C/rGO are all composed of a compressed semicircle in high frequency and an inclined line in low frequency. The diameter of the plot in the high-frequency can be attributed to the charge-transfer impedance (R_{ct}) in the interface of electrode and electrolyte. It is clear that the bmSi electrode possesses the largest Rct while that of bmSi@C is much lower and the Rct of bmSi@C/rGO is the smallest. Thus we can get the conclusion that carbon layer and reduced graphene oxide are of great helpful in improving electrical conductivity of the composite, which is very conductive to optimizing reversibility and rate performance.

4. Conclusions

We have successfully fabricated bmSi@C/rGO composite through two-step successive deposition process driven by electrostatic interactions. In this construction chitosan is selected as carbon source as well as bridge-charged to connect bmSi particles and graphene oxide through electrostatic interaction. In the as-prepared composite, carbon layer and reduced graphene oxide provide a double protective network. They are served as superior electrical conductors so as to improve the reversibility and rate performance of the composite. On the other hand, they are a buffer for the volume expansion of the bmSi particles in the lithiation/delithiation process and a safeguard for the structural and cyclical stability caused from the pulverization of silicon. When used as anode material, the composite shows outstanding cycle performance and rate capacity. It delivers a 935.77 mAh g^{-1} capacity and 71.9% capacity retention after 100 cycles. Therefore, the novel and compact electrostatic self-assembly here provides an effective way to fabricate a series of graphene wrapped carbon composites.

Acknowledgments

Appendix A. Supplementary data

Supplementary data associated with this article can be found, in the online version, at http://dx.doi.org/10.1016/j.electacta.2016.04.019.

References

[1] J.-M. Tarascon, M. Armand, Issues and challenges facing rechargeable lithium batteries, Nature 414 (2001) 359–367.
[2] V. Manev, I. Naidenov, B. Puresheva, P. Zlatilova, G. Pistoia, Electrochemical performance of natural Brazilian graphite as anode material for lithium-ion rechargeable cells, Journal of Power Sources 55 (1995) 211–215.
[3] Y. Yang, D. Chen, B. Liu, J. Zhao, Binder-free Si nanoparticle electrode with 3D porous structure prepared by electrophoretic deposition for lithium-ion batteries, ACS applied materials & interfaces 7 (2015) 7497–7504.
[4] H. Wu, Y. Cui, Designing nanostructured Si anodes for high energy lithium ion batteries, Nano Today 7 (2012) 414–429.
[5] Y. Xu, Y. Zhu, C. Wang, Mesoporous carbon/silicon composite anodes with enhanced performance for lithium-ion batteries, Journal of Materials Chemistry A 2 (2014) 9751.
[6] M.-S. Wang, Y. Song, W.-L. Song, L.-Z. Fan, Three-Dimensional Porous Carbon-Silicon Frameworks as High-Performance Anodes for Lithium-Ion Batteries, ChemElectroChem 1 (2014) 2124–2130.
[7] L.L. Tian, X.Y. Wei, Q.C. Zhuang, C.H. Jiang, C. Wu, G.Y. Ma, X. Zhao, Z.M. Zong, S.G. Sun, Bottom-up synthesis of nitrogen-doped graphene sheets for ultrafast lithium storage, Nanoscale 6 (2014) 6075–6083.
[8] R. Hu, W. Sun, Y. Chen, M. Zeng, M. Zhu, Silicon/graphene based nanocomposite anode: large-scale production and stable high capacity for lithium ion batteries, Journal of Materials Chemistry A 2 (2014) 9118.
[9] L. Wang, B. Gao, C. Peng, X. Peng, J. Fu, P.K. Chu, K. Huo, Bamboo leaf derived ultrafine Si nanoparticles and Si/C nanocomposites for high-performance Li-ion battery anodes, Nanoscale 7 (2015) 13840–13847.
[10] W. Wei, G. Wang, S. Yang, X. Feng, K. Mullen, Efficient Coupling of Nanoparticles to Electrochemically Exfoliated Graphene, Journal of the American Chemical Society (2015).
[11] M. Zhou, F. Pu, Z. Wang, T. Cai, H. Chen, H. Zhang, S. Guan, Facile synthesis of novel Si nanoparticles-graphene composites as high-performance anode materials for Li-ion batteries, Physical chemistry chemical physics: PCCP 15 (2013) 11394–11401.
[12] Y. Wen, Y. Zhu, A. Langrock, A. Manivannan, S.H. Ehrman, C. Wang, Graphene-Bonded and −Encapsulated Si Nanoparticles for Lithium Ion Battery Anodes, Small 9 (2013) 2810–2816.
[13] F. Zhang, X. Yang, Y. Xie, N. Yi, Y. Huang, Y. Chen, Pyrolytic carbon-coated Si nanoparticles on elastic graphene framework as anode materials for high-performance lithium-ion batteries, Carbon 82 (2015) 161–167.
[14] S. Yang, X. Feng, S. Ivanovici, K. Mullen, Fabrication of graphene-encapsulated oxide nanoparticles: towards high-performance anode materials for lithium storage, Angewandte Chemie 49 (2010) 8408–8411.
[15] H. Yang, Z. Hou, N. Zhou, B. He, J. Cao, Y. Kuang, Graphene-encapsulated SnO2 hollow spheres as high-performance anode materials for lithium ion batteries, Ceramics International 40 (2014) 13903–13910.
[16] M. Sangare, G.J. Fodjouong, X. Huang, Graphene-encapsulated silicon nanoparticles as an anode material for lithium-ion batteries, Mendeleev Communications 23 (2013) 284–285.
[17] X. Zhou, Y.-X. Yin, L.-J. Wan, Y.-G. Guo, Self-Assembled Nanocomposite of Silicon Nanoparticles Encapsulated in Graphene through Electrostatic Attraction for Lithium-Ion Batteries, Advanced Energy Materials 2 (2012) 1086–1090.
[18] S.N. Lim, W. Ahn, S.H. Yeon, S.B. Park, Preparation of a reduced graphene oxide wrapped lithium-rich cathode material by self-assembly, Chemistry, an Asian journal 9 (2014) 2946–2952.
[19] N. Lin, J. Zhou, L. Wang, Y. Zhu, Y. Qian, Polyaniline-assisted synthesis of Si@C/RGO as anode material for rechargeable lithium-ion batteries, ACS applied materials & interfaces 7 (2015) 409–414.
[20] Y. Shi, Y. Fu, H. Lv, J. Zhong, Z. Liu, D. Ma, W. Xue, Poly(methacrylic acid) microparticles coated with nanolayered chitosan and carbon nanotubes via electrostatic self-assembly for gatifloxacin delivery, Materials Letters 125 (2014) 198–201.
[21] W. Jiang, X. Chen, B. Pan, Q. Zhang, L. Teng, Y. Chen, L. Liu, Spherical polystyrene-supported chitosan thin film of fast kinetics and high capacity for copper removal, Journal of hazardous materials 276 (2014) 295–301.
[22] W.S.H.J.R.E. Offeman, Preparation of Graphitic Oxide, J. Am. Chem. Soc 80 (1958) 1339.
[23] G. Ramis, Y. Li, G. Busca, Ammonia activation over catalysts for the selective catalytic reduction of NO, and the selective catalytic oxidation of NH 3. FT-IR study, Catalysis Today 28 (1996) 373–380.
[24] B. Ma, A. Qin, X. Li, C. He, High tenacity regenerated chitosan fibers prepared by using the binary ionic liquid solvent (Gly·HCl)-[Bmim]Cl, Carbohydrate Polymers 97 (2013) 300–305.
[25] C. Chen, Q.-H. Yang, Y. Yang, W. Lv, Y. Wen, P.-X. Hou, M. Wang, H.-M. Cheng, Self-Assembled Free-Standing Graphite Oxide Membrane, Advanced materials 21 (2009) 3007–3011.
[26] A.C. Ferrari, J.C. Meyer, V. Scardaci, C. Casiraghi, M. Lazzeri, F. Mauri, S. Piscanec, D. Jiang, K.S. Novoselov, S. Roth, A.K. Geim, Raman Spectrum of Graphene and Graphene Layers, Physical Review Letters 97 (2006).
[27] J. Wu, X. Qin, H. Zhang, Y.-B. He, B. Li, L. Ke, W. Lv, H. Du, Q.-H. Yang, F. Kang, Multilayered silicon embedded porous carbon/graphene hybrid film as a high performance anode, Carbon 84 (2015) 434–443.
[28] S. Stankovich, D.A. Dikin, R.D. Piner, K.A. Kohlhaas, A. Kleinhammes, Y. Jia, Y. Wu, S.T. Nguyen, R.S. Ruoff, Synthesis of graphene-based nanosheets via chemical reduction of exfoliated graphite oxide, Carbon 45 (2007) 1558–1565.
[29] I. Hong, B. Scrosati, F. Croce, Mesoporous, Si/C composite anode for Li battery obtained by 'magnesium-thermal' reduction process, Solid State Ionics 232 (2013) 24–28.

[30] S. Fang, L. Shen, G. Xu, P. Nie, J. Wang, H. Dou, X. Zhang, Rational design of void-involved Si@TiO2 nanospheres as high-performance anode material for lithium-ion batteries, ACS applied materials & interfaces 6 (2014) 6497–6503.

[31] J.-Z. Wang, C. Zhong, S.-L. Chou, H.-K. Liu, Flexible free-standing graphene-silicon composite film for lithium-ion batteries, Electrochemistry Communications 12 (2010) 1467–1470.

[32] B. Lung-Hao Hu, F.Y. Wu, C.T. Lin, A.N. Khlobystov, L.J. Li, Graphene-modified LiFePO(4) cathode for lithium ion battery beyond theoretical capacity, Nature communications 4 (2013) 1687.

[33] W.-R. Liu, Z.-Z. Guo, W.-S. Young, D.-T. Shieh, H.-C. Wu, M.-H. Yang, N.-L. Wu, Effect of electrode structure on performance of Si anode in Li-ion batteries: Si particle size and conductive additive, Journal of Power Sources 140 (2005) 139–144.

[34] R. Epur, M.K. Datta, P.N. Kumta, Nanoscale engineered electrochemically active silicon–CNT heterostructures-novel anodes for Li-ion application, Electrochimica Acta 85 (2012) 680–684.

[35] H. Tian, X. Tan, F. Xin, C. Wang, W. Han, Micro-sized nano-porous Si/C anodes for lithium ion batteries, Nano Energy 11 (2015) 490–499.